Energy & Environmental Science

PAPER

View Article Online
View Journal



# An inversion layer at the surface of n-type iron pyrite†

Cite this: DOI: 10.1039/c3ee43169j

Moritz Limpinsel,[a] Nima Farhi,[b] Nicholas Berry,[c] Jeffrey Lindemuth,[d] Craig L. Perkins,[e] Qiyin Lin[f] and Matt Law*[abf]

Numerical modeling of Hall effect data is used to demonstrate the existence of a conductive inversion layer at the surface of high-quality n-type single crystals of iron pyrite (cubic $FeS_2$) grown by a flux technique. The presence of the inversion layer is corroborated by Hall measurements as a function of crystal thickness and photoemission spectroscopy. This hole-rich surface layer may explain both the low photovoltage of pyrite solar cells and the widely-observed high p-type conductivity of polycrystalline pyrite thin films that have together perplexed researchers for the past thirty years. We find that the thickness and conductivity of the inversion layer can be modified by mechanical and chemical treatments of the pyrite surface, suggesting that it may be possible to eliminate this hole-rich layer by passivating surface states and subsurface defects. Furthermore, modeling of the high-temperature electrical conductivity shows that the electronic band gap is 0.80 ± 0.05 eV at room temperature (compared to 0.94 eV according to optical transmission data), confirming that photovoltages of ~500 mV should be attainable from pyrite under solar illumination.

Received 21st September 2013
Accepted 28th March 2014

DOI: 10.1039/c3ee43169j

www.rsc.org/ees

**Broader context**

Iron pyrite (cubic $FeS_2$) is an earth-abundant, non-toxic semiconductor that can produce large photocurrents in solar cells, but the surprisingly small photovoltage generated by this material (<0.2 V) has limited its cell efficiency to ~3% and prevented its commercial development. Debate about the origin of pyrite's low voltage has occurred intermittently over the past 30 years, intensifying recently as a growing number of researchers reexamine this intriguing material. Here, we use electrical measurements of high-purity single crystals to show that there is a thin, conductive inversion layer (a p-type layer) on the surface of n-type pyrite. Conductive surface layers are well known for other optoelectronic materials, including InN and HgCdTe. Tunneling of charge carriers across pyrite's thin inversion layer may result in voltage losses that account for the low voltage of pyrite solar cells. Moreover, the p-type surface can explain why the great majority of pyrite thin films are reported to be p-type regardless of synthesis technique or composition. We show that surface treatments such as chemical etches can substantially reduce the conductivity of the inversion layer. This suggests that passivating the surface states believed to create the surface layer is critical to boosting the efficiency of pyrite solar cells.

## 1. Introduction

Iron pyrite (cubic $FeS_2$) seems a nearly ideal absorber layer for scalable thin-film solar cells due to its suitable band gap (widely accepted to be ~0.95 eV), high absorption coefficient ($\alpha > 10^5$ cm$^{-1}$ for $h\nu$ > 1.3–1.4 eV), sufficient minority carrier diffusion length, practically infinite elemental abundance, and low toxicity. Although large short-circuit photocurrent densities (>30 mA cm$^{-2}$) have been reported from pyrite single crystals,[1,2] all pyrite photocells to date suffer from a low open-circuit voltage ($V_{OC}$) that limits their power conversion efficiency to ~3%.[3] Proposed explanations for the low $V_{OC}$ include bulk phase impurities,[4,5] a high concentration of bulk point defects (particularly sulfur and iron vacancies),[3,6,7] a metallic FeS-like surface layer,[8,9] and surface states that generate a hole-rich surface inversion/accumulation layer,[10,11] possibly having a reduced band gap compared to bulk pyrite.[12] We have recently argued that the explanation most consistent with the main experimental data (*i.e.*, high photocurrents but low photovoltages from pyrite single crystals, as well as high p-type conductivity of pyrite thin films regardless of composition or preparation method) is that pyrite has a hole-rich surface inversion/accumulation layer that results in a leaky and/or

[a]Department of Chemistry, University of California, Irvine, CA 92697, USA
[b]Dept. of Chemical Engineering and Materials Science, University of California, Irvine, CA 92697, USA
[c]Department of Physics and Astronomy, University of California, Irvine, CA 92697, USA
[d]Lake Shore Cyrotronics, Inc., 575 McCorkle Blvd, Westerville, OH 43082, USA
[e]National Renewable Energy Laboratory, Golden, CO, USA
[f]Laboratory for Electron and X-ray Instrumentation, University of California, Irvine, CA 92697, USA. E-mail: matt.law@uci.edu

† Electronic supplementary information (ESI) available: Na–S phase diagram, pyrite single crystal XRD structure refinement, X-ray tomography results, certificates of analysis, additional XRD and SEM data, modeling results, optical, electrical and magnetoresistance data, and a summary of literature results on the band gap of pyrite. See DOI: 10.1039/c3ee43169j

small potential energy barrier at the surface.[11–13] Here we demonstrate the existence of this inversion layer on the surface of high-quality n-type pyrite single crystals using variable-temperature Hall effect and valence band photoemission measurements. We show that the surface layer, which may have a band gap significantly smaller than that of bulk pyrite, is electrically conductive and dominates transport when the number of surface holes becomes substantially larger than the number of bulk electrons (*i.e.*, for thin samples and/or low temperatures). We find that the conductance of the inversion layer can be altered by physicochemical treatments of the pyrite surface, suggesting that it may be possible to eliminate this hole-rich layer and boost the $V_{OC}$ of pyrite solar cells by passivating surface states and near-surface defects.

## 2. Results and discussion

Pyrite single crystals were synthesized in sodium polysulfide flux[14,15] by heating an evacuated quartz ampoule containing a crucible filled with high-purity iron, sulfur, and $Na_2S$ to 780 °C and cooling to room temperature over ~29 hours (see the Experimental section). $Na_2S$-sulfur is an excellent flux for pyrite crystallization because it is liquid over a wide range of composition and temperature (see ESI Fig. S1†), shares a common anion with pyrite, and features a cation that does not incorporate into pyrite to any significant degree (<200 ppb according to secondary ion mass spectrometry measurements, see below). Our particularly simple implementation of this flux method produces larger and purer, crystallographically perfect pyrite crystals more quickly than alternative approaches such as chemical vapor transport (CVT). The high purity of these crystals proved critical for revealing *via* Hall effect measurements a hole-rich layer at the surface of pyrite. We believe that the tunneling of carriers across this layer may cause the low voltage of pyrite photocells, as described in some detail below.

### 2.1. Structural and elemental characterization

Fig. 1 shows basic structural characterization of the crystals. The flux synthesis produces highly-faceted but noncubic crystals with a typical size of 8 × 8 × 6 mm (limited by the size of our crucibles). Most of the facets are optically flat with a golden mirror finish, but some have a large density of macro-steps and small terraces (Fig. 1a). High-resolution synchrotron powder XRD patterns of crushed crystals index to pyrite with a room-temperature lattice constant of 5.41741 ± 0.00087 Å and show no trace of other crystalline or amorphous phases (Fig. 1b). Likewise, Raman spectra feature only sharp pyrite peaks (Fig. 1c). Slabs were cut with a diamond saw parallel to prominent facets and polished to ~2 nm RMS roughness using SiC paper and a series of slurries (see Experimental). Wide-angle $2\theta$–$\omega$ XRD scans show the slabs are single crystals with (111) or, less often, (210) orientation (Fig. 1e). (111) rocking curve peak widths of 6–9 arcseconds indicate that the pyrite slabs have a very high degree of crystalline perfection, comparable to commercial silicon wafers (Fig. 1f). To determine whether the crystals are in fact single crystalline throughout their volume, we acquired $2\theta$–$\omega$ and pole figure data of slabs cut in several orthogonal orientations and found that nearly all specimens are indeed highly-perfect single crystals (data not shown), although a few samples showed evidence of a small number of slightly misoriented grains in pole figures. Single crystal X-ray diffraction of small crystallites (~0.2 mm on a side) detached from the as-grown crystals showed very high-quality single crystal pyrite patterns (see Fig. S2† and discussion). Crystal structure refinement yielded site occupancy factors of 1.00 ± 0.04 for both Fe and S, indicating a stoichiometry of $FeS_{2.0}$ within the error of the refinement. This agrees well with a sulfur-to-iron ratio of 1.988 ± 0.03 (*i.e.*, $FeS_{2.0}$ within experimental error) determined by closed-vessel inductively coupled plasma optical emission spectroscopy (ICP-OES) analysis of an as-grown crystal, particularly considering the tendency for sulfur to be lost to the gas phase during pyrite digestion.[16] Overall, our results show that the flux synthesis produces large, high-quality, and stoichiometric pyrite single crystals.

A disadvantage of the flux synthesis is that the pyrite crystals always contain macroscopic voids. These voids are clearly visible by eye upon sectioning an as-grown crystal. X-ray tomography was employed to image the voids in several as-grown crystals. 3D reconstructions show that some regions of each crystal contain localized networks of elongated and globular voids (Fig. S3 and Movie S1†). Some of the voids open to the external surface of the crystal, while others are closed. The density of several crystals was measured by helium pycnometry to be 4.904(3)–4.959(3) g $cm^{-3}$, or 97.9–99.0% of the theoretical density of pyrite (5.011 g $cm^{-3}$ at room temperature). Since pycnometry measures the skeletal volume (*i.e.*, the volume of the crystal plus any voids inaccessible to He), we conclude that only a relatively small fraction of the void volume is closed. Crucially, the top ~1 mm of most crystals is completely free of voids, while the void density increases toward the bottom of the crystal (*i.e.*, where the crystal touches the crucible). All electrical and optical measurements described in this paper used void-free slabs in order to avoid potential complications from empty volume effects.

The bulk elemental composition of the crystals was determined by glow discharge mass spectrometry (GDMS), instrumental gas analysis (IGA), and secondary ion mass spectroscopy (SIMS), as described in the Experimental section. GDMS provides a full elemental survey (Li–U) with ppb–ppm detection limits, while IGA measures gas-forming elements (O, C, N, H, S) over a wide dynamic range (ppm to percent levels). SIMS is a surface probe that samples a much smaller amount of material than either GDMS or IGA (~0.5 μg *versus* >10 mg). Table 1 lists all impurities detected in the crystals by the three techniques. Based on the GDMS/IGA data, the total impurity content of the crystals excluding oxygen, carbon and hydrogen is ~25 ppm, with the only elements above 1 ppm being Cr (6.4 ppm), B (6.3 ppm), Si (4.2 ppm), Na (4.2 ppm), and Cl (1.1 ppm). Chromium is a known impurity in our iron starting material (see Fig. S4–S7† for information on the impurity content of precursors) and can be eliminated by using commercial batches of iron that are free of chromium. Since the sodium was largely removed by thoroughly rinsing crushed crystals in water, we

 

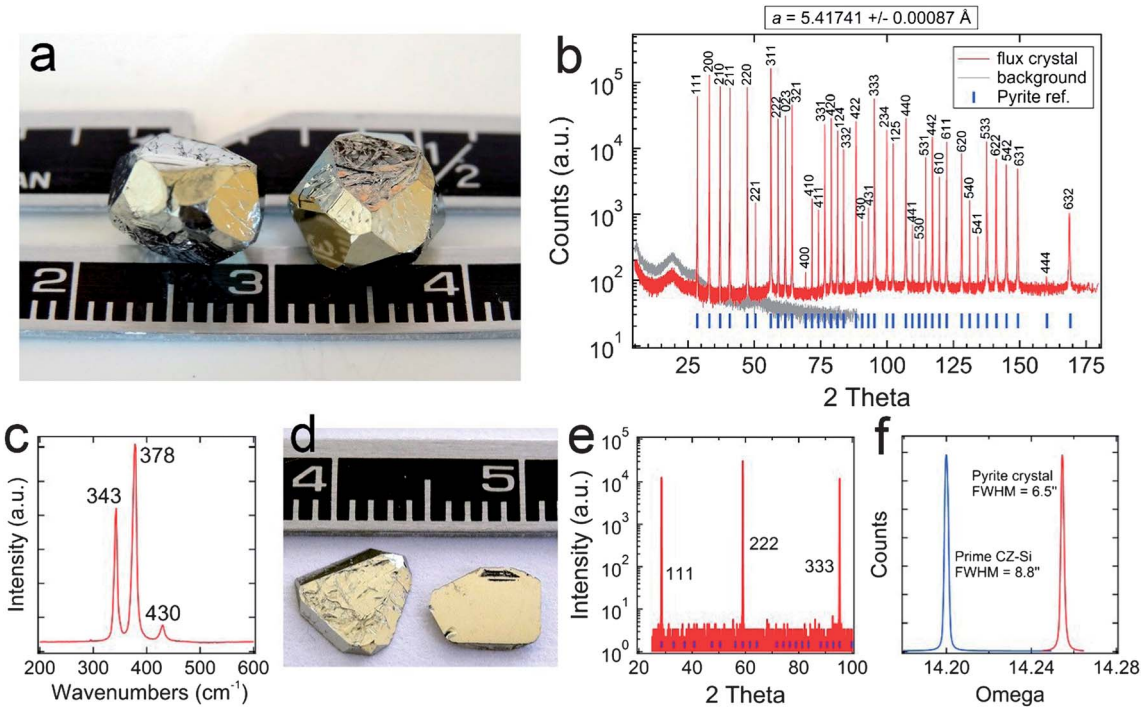


Fig. 1 Pyrite single crystals grown in a $Na_2S$-sulfur flux. (a) Photograph of two as-grown crystals. Scale is in centimeters. (b) Synchrotron XRD pattern of a powdered crystal on a log scale. All 39 reflections index to pyrite and no other phases are detected. A linear least squares fit of the data gives a cubic lattice parameter of 5.41741 ± 0.00087 Å at room temperature. The background pattern is for an empty capillary tube. Small blue bars near the *x*-axis denote the pyrite reference peaks. (c) Typical Raman spectrum of a pyrite slab. All peaks correspond to pyrite.[13] (d) Photograph of pyrite slabs showing a heavily stepped as-grown facet (left) and a polished facet (right). (e) $2\theta-\omega$ XRD scan on a log scale of a polished slice with (111) orientation. Small blue bars near the *x*-axis denote the pyrite reference peaks. (f) (111) rocking curves for a pyrite slab and a prime grade CZ-grown Si wafer. The pyrite slab shows a FWHM of 6.5 arcseconds, compared to 8.8 arcseconds for the Si wafer.

Table 1 Elemental analysis of pyrite flux crystals by GDMS, IGA, and SIMS[a]

| Element | GDMS/IGA concentration (ppm at.) | SIMS concentration (ppm at.) |
|---|---|---|
| O | 1775[b] | 1–4 |
| C | 533[b] | 1–2 |
| N | DL (<28) | NM |
| H | ?[c] | (15, 52, 560)[d] |
| Cr | 6.4 | (1, 3, 82)[d] |
| B | 6.3 | NM |
| Si | 4.2 | NM |
| Na | 4.2[b] | <0.006–0.2 |
| Cl | 1.1 | 0.05–0.2 |
| Ni | 0.9 | NM |
| Ca | 0.4 | <0.003–0.2 |
| Al | 0.4 | 0.07–0.2 |
| Mg | 0.3 | <0.002–0.008 |
| P | 0.1 | NM |
| F | DL (<1) | <0.03–0.2 |
| K | DL (<0.1) | <0.0004–0.3 |

[a] Data for crystals grown in pBN crucibles. [b] Oxygen, carbon, and sodium are present on the crystal surface, with very little in the lattice. [c] Hydrogen could not be accurately measured by IGA. [d] Values listed for three different crystals to show variability. All unlisted elements (Li–U) were below GDMS detection limits (0.01–0.5 ppm at. for most elements). SIMS data are average bulk values (>500 nm from the crystal surface). DL = below detection limit; NM = not measured.

believe that sodium is present only on the surface of the crystals (as residual flux) and not as substitutional or interstitial impurities in the pyrite lattice. SIMS data confirm this interpretation (see below). The origin of the boron, silicon, and chlorine contamination is less clear. Boron is present regardless of whether pBN or alumina crucibles are used in the syntheses, so it must originate from the $Na_2S$ precursor or, less likely, the quartz ampoule. Silicon probably comes from the quartz. If we disregard Na, our crystals are 99.998% pure on a "metals" basis, making them the purest pyrite crystals yet reported.[17–21]

Although the metal levels are very low, high concentrations of oxygen (1775 ppm) and carbon (533 ppm) were detected by IGA, and we could not reliably quantify the hydrogen content by IGA due to instrument complications from sulfur. Oxygen, carbon, and hydrogen could have important electronic effects if these elements are in the lattice rather than on the surface of the crystals. We used SIMS depth profiling to verify the concentration of oxygen, carbon, and a group of other trace elements (H, Cr, Al, F, Cl, Na, K, Mg, and Ca) in several locations on three different pyrite crystals. As seen in Fig. 2, SIMS profiles show that the concentration of oxygen and carbon is only 1–5 ppm in the bulk of the crystals, much lower than the values determined from IGA. The higher concentration of oxygen and carbon near the surface of the crystals – which probably results mainly from surface particle contamination (unavoidable for samples prepared in non-UHV conditions) – is insufficient to

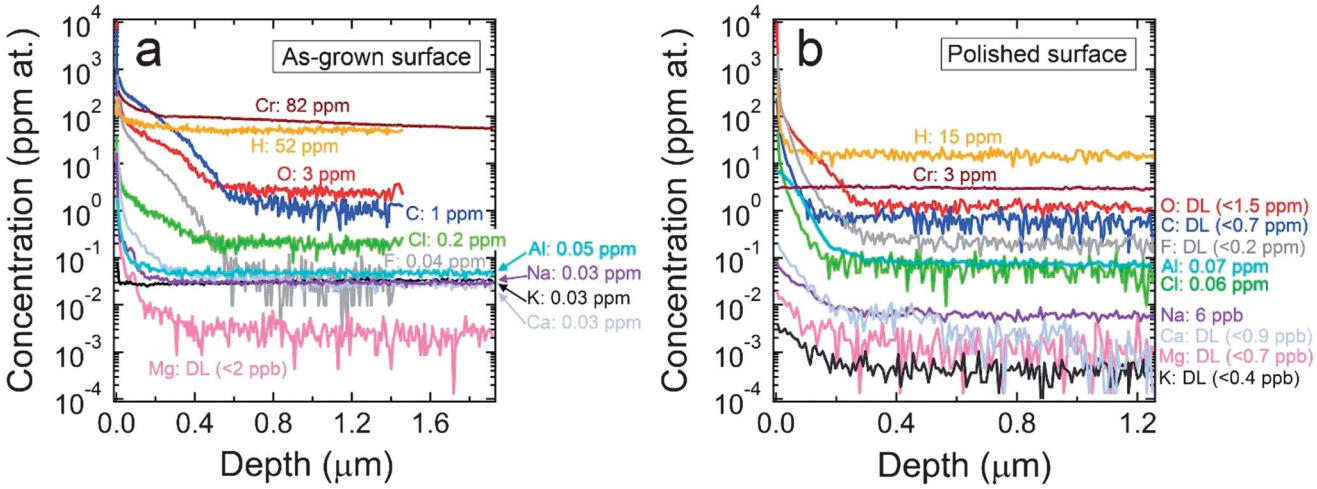


Fig. 2 SIMS depth profiles of (a) an as-grown surface and (b) a polished surface of two different pyrite crystals. DL = below detection limit.

reconcile the IGA and SIMS results, implying sources of oxygen/carbon that the SIMS experiments do not detect. Based on these combined data, we conclude that the oxygen and carbon contamination sits mostly on the surface of the crystals and is present in the pyrite lattice only in ppm concentrations.

SIMS also shows a substantial, sample-dependent concentration of hydrogen (15, 52, and 560 ppm in three different samples) and chromium (1, 3, and 82 ppm) in the pyrite bulk. Hydrogen is a ubiquitous impurity that may originate from our $H_2$-reduced iron precursor, incompletely-dried $Na_2S$ or sulfur precursors, or several other potential sources. Hydrogen may act as an electronic dopant in pyrite. Chromium is from the iron precursor, as mentioned above. All other elements monitored by SIMS were below ~0.2 ppm, in rough agreement with GDMS results. The variation in impurity concentration from sample to sample probably reflects variations in precursor purity and sample processing, but we cannot rule out the possibility that the crystals have an inhomogeneous impurity distribution. Future work will assess the homogeneity of the crystals at different length scales. Based on the combined GDMS, IGA, and SIMS data, we conclude that (i) our crystals have a total lattice impurity content of ~80 ppm (assuming ~52 ppm of hydrogen on average), making them ~99.992% pure overall, (ii) hydrogen is the major extrinsic impurity, and (iii) surface particle contamination is responsible for the high levels of oxygen and carbon detected by IGA. Although our crystals are quite pure, efforts are underway to improve their total elemental purity to better than 99.999% for ongoing doping and transport studies.

### 2.2. Hall effect studies

Hall effect data were collected on pyrite (111) and (210) slabs in a van der Pauw geometry over a temperature range of 40–700 K (see Experimental). Fig. 3 plots the conductivity $\sigma$ and the absolute value of the Hall coefficient $|R_H|$ *versus* inverse temperature for a typical sample. The conductivity decreases by a factor of $\sim 10^8$ with decreasing temperature and shows three distinct linear regions of progressively smaller activation energy: (I) $E_a \sim 375$ meV for $T > 500$ K; (II) $E_a \sim 163$ meV for 350 K > $T$ > 130 K; (III) $E_a \sim 24$ meV for $T < 90$ K. We assign region I as the intrinsic region, where the activation energy is related to the (high-temperature) band gap of pyrite. Region I is discussed in more detail in Section 2.3. In region II, the crystal is clearly n-type (large negative value of $R_H$) and transport is dominated by the ionization of donor states. Since $n \gg p$ in this extrinsic region, the Hall coefficient simplifies to $R_H = -1/ne$ and the Hall data can be used to estimate the free electron density $n$, mobility $\mu_e$, donor concentration $N_D$, and donor energy $E_D$. At 300 K, $n = 5 \times 10^{15}$ cm$^{-3}$ and $\mu_e = 245$ cm$^2$ V$^{-1}$ s$^{-1}$.

We consider two limiting cases for determining $E_D$ and $N_D$ from the slope of $R_H(T)$ in region II. The slope in this region corresponds to an activation energy of ~195 meV for $n(T)$. We note that the $E_a$ of $\sigma(T)$ is somewhat different (~165 meV) because $\sigma$ is the product of two temperature-dependent quantities, $n(T)$ and $\mu_e(T)$, while $R_H(T)$ in the unipolar region depends only on $n(T)$. If we first assume that the crystals are uncompensated ($N_A/N_D = 0$, where $N_A$ is the concentration of acceptors), then the Fermi level is located about halfway between $E_D$ and the conduction band edge $E_C$, such that $(E_C - E_D)/2 \approx$ 195 meV. In this case, the donor ionization energy $E_C - E_D$ is ~390 meV and, using the approximation $N_D \sim ne^{(E_C - E_D)/2k_BT}$, we find $N_D = 9 \times 10^{18}$ cm$^{-3}$ (equivalent to ~120 ppm). However, it is extremely unlikely for a compound semiconductor to be completely uncompensated. At ~60% compensation (see Fig. S8† for justification of this value), the Fermi level is essentially equal to the donor level, making $E_C - E_D \sim 195$ meV. In this case, the donor ionization energy determined from $R_H(T)$ is approximately 195 meV, while $N_D$ remains unchanged. Since including compensation changes little other than the energy of the donor state, we assume zero compensation in most of the remainder of this paper. We believe that the donor is probably a native defect (most likely a sulfur vacancy or vacancy cluster), since hydrogen is the only extrinsic impurity with a concentration higher than $\sim 10^{18}$ cm$^{-3}$ yet the Hall data show no clear correlation to the hydrogen concentration. A graph of electron

 

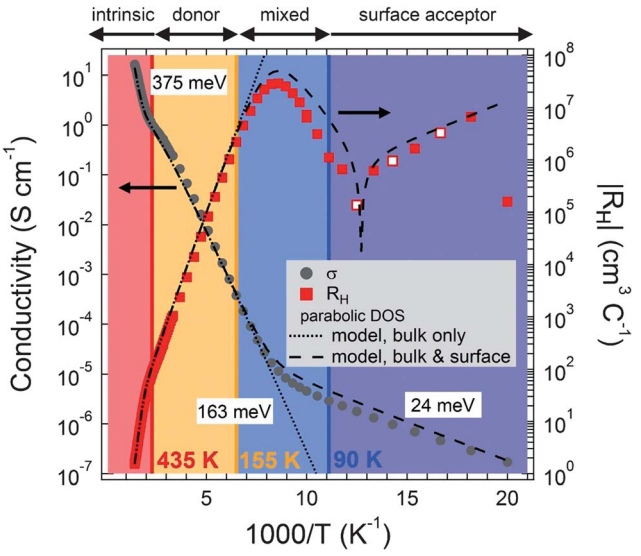


Fig. 3 Raw Hall effect data ($\sigma$ and $|R_H|$) for a pyrite (111) slab with a thickness of 1040 μm. The conductivity shows three linear regions with activation energies of 375 meV, 163 meV, and 24 meV, respectively. The Hall coefficient exhibits unusual behavior, including a minimum at ~120 K and a sign change from negative (electron dominant) to positive (hole dominant) at ~80 K. Red squares indicate negative values of $R_H$, while red and white squares are positive values. The sign of $R_H$ varies at low temperature because the Hall voltage $V_H$ is very small in this regime. The high-temperature data can be fit with a model that considers only a homogeneous crystal with a single donor (dotted traces). A three-layer model (n-type bulk plus p-type surface on each side of the crystal) is needed to fit the data over the entire temperature range (dashed traces; see Experimental section). This fit uses the normal parabolic DOS($E$) functions, the free electron approximation, and the Fermi–Dirac distribution function, assuming zero compensation of bulk and surface. See Fig. S8† for fits that include the bulk compensation ratio as a free parameter. Using instead numerical DOS($E$) values obtained from density functional theory (DFT) calculations of the pyrite band structure[22] results in fits that are systematically better at low temperature but worse at high temperature (see Fig. S10 for the fits,† Fig. S11 for a comparison of the two types of DOS($E$) functions used in the modeling, and Fig. S12† for a comparison of modeling results using the two DOS($E$) functions). Fit parameters are shown in Table 2. The sample is intrinsic at high temperatures (red region). With decreasing temperature, transport becomes dominated by bulk electrons (yellow), enters a transition region of mixed electron and hole conduction (blue), and then becomes dominated by surface holes as the bulk electrons are frozen out (gray).

density and mobility that assumes (necessarily but wrongly) the validity of the single carrier approximation for all temperatures is shown for illustration in ESI (Fig. S9†). The mobility in region II varies with temperature as $T^{-2.0}$ to $T^{-2.5}$, implying that phonon scattering limits the mobility at intermediate temperatures, as it does in most high-quality single crystals. The mobility peaks at values up to 1930 $cm^2\ V^{-1}\ s^{-1}$ at ~120 K before appearing to decrease at lower temperatures. However, as discussed below, conduction from 90–155 K is mixed between bulk electrons and surface holes, making $R_H \neq -1/ne$. As a result, the peak electron mobility in Fig. S9† is probably underestimated and the mobility values in this intermediate range of temperatures have no clear physical meaning.

Table 2 Fit parameters used in Fig. 3 and S10†

| Parameter (unit) | Parabolic DOS | DFT DOS |
|---|---|---|
| $N_D$ ($cm^{-3}$) | $6.3 \times 10^{18}$ | $5.6 \times 10^{19}$ |
| $E_C - E_D$ (meV) | 390 | 380 |
| $N_A$ ($cm^{-3}$) | $2.2 \times 10^{20}$ | $4.5 \times 10^{19}$ |
| $E_A - E_V$ (meV) | 50 | 50 |
| $E_{gap,300\ K}$ (meV) | 700 | 700 |
| $\mu_h$ ($cm^2\ V^{-1}\ s^{-1}$) | 2.5 | 2.5 |
| $d_s$ (nm) | 4.4 | 4.4 |

The Hall coefficient exhibits unusual behavior at temperatures below ~155 K. Instead of showing the expected monotonic increase in magnitude due to carrier freeze out, $R_H$ of the pyrite samples reaches a minimum at ~120 K, increases, and then passes through zero at ~80 K and changes sign from negative (electron dominant) to positive (hole dominant) at lower temperatures. This sign change appears as a cusp in $|R_H(T)|$ in Fig. 3. Such an $R_H$ extremum and sign reversal cannot occur in a doped or compensated semiconductor away from the intrinsic region *unless* (a) the mobility of holes becomes many orders of magnitude larger than that of electrons at low temperature, (b) the mechanism of charge transport changes from band conduction to some form of hopping below ~155 K, or (c) conduction in a p-type surface inversion layer dominates the low-temperature transport.

To test premise (a), we calculated $R_H(T)$ self-consistently for widely-varying combinations of dopant density, dopant ionization energy, and carrier mobility and found that low-temperature $R_H$ sign changes can occur only when $\mu_e(T)$ or $\mu_h(T)$ is unphysical, such as when $\mu_h(T)$ increases exponentially by many decades with decreasing temperature (Fig. S13†). We conclude that the observed $R_H(T)$ behavior must be due to either a transition to hopping transport (premise b) or surface conduction (premise c).

Conduction by hopping between localized states in a compensated single crystal can cause unusual $R_H$ behavior – including extrema and possibly sign reversals – that might in principle explain our $R_H(T)$ data.[23,24] Only a few reports have presented non-monotonic $R_H(T)$ data from pyrite.[18,25–27] Most notably, Tomm *et al.* observed a maximum in $|R_H|$ similar to ours, but with no sign reversal.[28] These authors attributed the $R_H$ turnover to a transition to hopping conduction at lower temperatures, without providing evidence to support this interpretation. Various types of hopping transport have also been reported recently in single-crystal pyrite nanostructures[29] and mixed-phase pyrite thin films containing metallic Fe grains.[30] To test for hopping conduction in our crystals, we first determined the temperature dependence of the low-temperature resistivity (region III in our notation). The resistivity $\rho$ of a single crystal typically takes the form $\rho(T) = \rho_0 \exp[(T_0/T)^p]$, where $p = 1$ can indicate either band conduction or nearest-neighbor hopping, $p = 1/2$ usually corresponds to Efros–Shklovskii variable range hopping (ES VRH), and $p = 1/4$ is characteristic of Mott variable range hopping.[24] To determine the value of $p$, we linearized $\rho(T)$ using the logarithmic derivative method described in ref. 30, giving

$\ln\left(-\frac{d(\ln \rho)}{d(\ln T)}\right) = \text{constant} - p \ln(T)$ (a derivation of this equation can be found in the ESI†). Fits of the low-temperature resistivity data yield $p \approx 0.53$ from 40–100 K, consistent with ES VRH (see Fig. S14†). In Gaussian cgs units, $T_0 = 2.8e^2/(\kappa a k_B)$, where $\kappa$ is the dielectric constant of pyrite ($\kappa = 20.5$) (ref. 31) and $a$ is the characteristic radius of the localized state participating in VRH. Given the limiting values of $E_D$ extracted from $R_H(T)$ (*i.e.*, $E_C - E_D = 0.390$ eV for zero compensation and $E_C - E_D = 0.195$ eV for finite compensation) and assuming an effective electron mass of $0.45m_e$,[22] our samples have $a = \hbar/\sqrt{2mE_D} = 4.6 - 6.6$ Å and thus $T_0 = 3480$–$4920$ K.[24] Note that this $a$ is smaller than the Bohr radius of electrons in pyrite ($a_{Bohr} \sim 23$ Å)[22] because the state radius decreases as $E_D^{-1/2}$, making deep donors smaller than shallow donors. Fits to the data from four crystals give $T_0 = 3550$–$6350$ K (Fig. S14†), in reasonable agreement with the value expected from ES VRH theory. We conclude that the low-temperature $\rho(T)$ data are generally consistent with ES VRH. However, hopping in single crystals, and especially VRH, usually occurs at much lower temperatures and with significantly smaller activation energies than is observed here.

We therefore sought to confirm ES VRH transport by measuring the dependence of the transverse magnetoresistance (MR = $[100(\rho(H) - \rho(0))/\rho(0)]$) on magnetic field and temperature. If conduction in a doped semiconductor is due to band transport rather than hopping, the resistivity should have a weak parabolic dependence on the magnetic field $H$, *i.e.*, $\rho(H) \approx \rho_0[1 + \mu^2(\mu_0 H)^2]$, when the field is weak (*i.e.*, $|\mu\mu_0 H| < 1$), where $\mu$ is the majority carrier mobility and $\mu_0$ is the magnetic permeability.[32] On the other hand, a characteristic feature of any type of hopping conduction is a large positive MR that increases exponentially with the strength of the magnetic field as

$$\rho(H) = \rho_0 \exp(AH^m), \quad (1)$$

where the value of $m$ and the form of $A$ depend on $H$.[24,33] The large positive MR is due to compression of the wavefunctions of localized states by the field that causes a rapid decrease in overlap between the tails of these states. For nearest-neighbor hopping in weak magnetic fields (*i.e.*, when the magnetic length $\lambda = [c\hbar/eH]^{1/2}$ is much larger than the characteristic radius of the impurity state, $m = 2$ and $A = 0.036ae^2/Nc^2\hbar^2$, where $N$ is the impurity concentration.[24] Since $\lambda \geq 85$ Å and $a \leq 6.6$ Å for our samples, the condition $\lambda \gg a$ is satisfied and the weak-field regime applies. A second condition for weak-field hopping MR is light to moderate doping of the semiconductor (*i.e.*, $Na^3 < 1$).[24] Using $N \sim 10^{19}$ cm$^{-3}$ for our crystals, we find $Na^3 \sim 0.001$–$0.003$, well within the range of validity of this equation. Using eqn (1) with weak-field values for $m$ and $A$, we predict only a very small MR of ~0.04% at our maximum field of 90 kOe. An even smaller MR (0.0007–0.0032%) is expected if ES VRH is the conduction mechanism at low temperature (see eqn (2) below).

Fig. 4 shows typical magnetoresistance data for a pyrite crystal at 70 K and 300 K. The MR is weak and positive at these and all other temperatures measured (30–300 K). The maximum value of the MR at 70 K is ~0.3%, which is ~8 times larger than expected for nearest-neighbor hopping and >95 times larger than expected for ES VRH. We find that the 70 K data can be fit equally well to a parabolic (band transport) or exponential (ES VRH; see eqn (2)) field dependence, but the extracted values of $\mu$ (63 cm$^2$ V$^{-1}$ s$^{-1}$) and $T_0$ (106 000–278 000 K) are unreasonably large (Fig. S15†). We conclude that $\rho(H)$ obeys neither expression and cannot be used to distinguish between band and hopping conduction in these samples. The fact that even the 300 K MR data fit well to an exponential, hopping-type function suggests that $\rho(H)$ is of limited use in determining the transport mechanism when the MR is small and positive.

The temperature dependence of the MR is also inconsistent with hopping. The typical temperature dependence of MR for ES VRH is:

$$\rho(H) = \rho_0 \exp[(ta^4/\lambda^4)(T_0/T)^{3/2}], \quad (2)$$

with $t = 0.0015$.[24] Using $a = 4.6$–$6.6$ Å and $T_0 = 3480$–$4920$ K, eqn (2) predicts the MR to increase by less than 0.01% from 100 K to 30 K at our strongest field (90 kOe). Plots of MR *vs.* $T$ from 30–300 K are shown in Fig. S16.† Although the low-temperature (<100 K) data are too scattered to reliably determine the temperature dependence of MR at weaker fields, at the strongest field the MR increases with decreasing temperature in qualitative agreement with eqn (2). However, fits to the data yield unreasonably large values for $T_0$ on the order of $10^5$ K. Based on this lack of quantitative agreement, we conclude that the temperature dependence of MR does not support hopping transport.

Overall, the $\rho(T)$ and $\rho(H)$ data are inconsistent with each other and unable to provide a firm conclusion about the existence of hopping transport in these pyrite crystals. The $\rho(T)$ analysis supports ES VRH transport, but MR($H$) cannot be explained by simple hopping or band conduction and MR($T$) is inconsistent with hopping. A more definitive conclusion *could* be obtained by determining whether the low-temperature resistivity shows an exponential dependence on the concentration of impurity states, but so far it has not proved possible to control the dopant concentration in pyrite to the degree needed for such a study. Regardless of whether hopping occurs, the

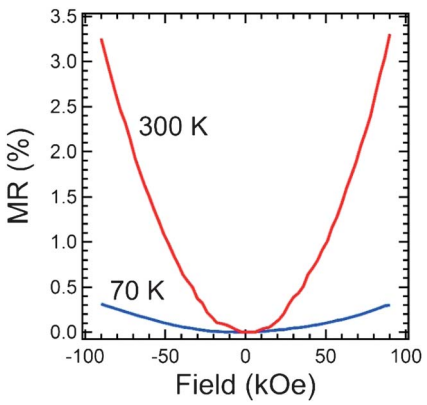


Fig. 4 Transverse magnetoresistance [100($\rho(H) - \rho(0)$)/$\rho(0)$] of a pyrite single crystal at 70 and 300 K in fields up to 90 kOe.

results we present below establish beyond doubt the existence of a conductive inversion layer at the surface of pyrite. The open question is then whether carriers in this surface layer move by hopping, conventional band transport, or perhaps even impurity band transport at low temperature.

We can quantitatively account for the Hall behavior of our pyrite crystals (*e.g.*, Fig. 3) by supposing that conduction is by a p-type surface layer in parallel with the n-type bulk of the crystal. The surface layer is an inversion layer caused by large upward band bending at the surface of the crystal. The origin of this band bending is discussed below. To model the Hall data, the crystal can be thought to consist of three layers: the bulk and a surface layer on each side of the crystal. Our model follows the approach of Petritz[34] and assumes a single donor level in the bulk and a single acceptor level in the surface layer (see Experimental section). Nonzero compensation in the bulk was also considered in some modeling fits. We calculate $E_F(T)$ self-consistently from the semiconductor charge neutrality condition and then determine $n(T)$ and $p(T)$ in all layers, while the mobilities are inputs to the model parameterized from the Hall data in the unipolar regions. The dotted traces in Fig. 3 show a simultaneous fit of the high-temperature $\sigma$ and $R_H$ data by considering only the bulk (zero compensation), without the surface layers. This fit is good at temperatures above the $|R_H|$ maximum, but of course cannot capture the unusual low-temperature behavior. Including the surface layers in the model results in a good global fit over the entire temperature range (dashed traces). Parameters used in the fits in Fig. 3 and S10,† including estimates of the density and ionization energy of both the donor and acceptor, are listed in Table 2 and are physically reasonable. Using parabolic DOS($E$) functions in the model results in the following typical values for the parameters: $N_{D,bulk} = 6.3 \times 10^{18}$ cm$^{-3}$; $E_C - E_D = 390$ meV; $E_A - E_V = 50$ meV; $d_s = 4.4$ nm; $\mu_h = 2.5$ cm$^2$ V$^{-1}$ s$^{-1}$. The surface acceptor density $N_{A,surface}$ depends on surface preparation and varies in the range of $10^{19}$–$10^{21}$ cm$^{-3}$. See Fig. S17† for typical model outputs specific to the bulk and surface layers. This model provides a simple explanation for the existence of the maximum and sign reversal in $|R_H|$: bulk conduction of electrons dominates at temperatures higher than the maximum (giving $R_H < 0$), while surface conduction of holes dominates at temperatures lower than the maximum (and gives $R_H > 0$). The activation energy of $\sigma$ at $T < 90$ K (*i.e.*, in region III) may correspond to the ionization of holes from a shallow surface acceptor into the valence band. At temperatures close to the $|R_H|$ maximum, bulk and surface conduction are of similar importance, giving rise to a regime of mixed transport between bulk electrons and surface holes. Spatial separation of these charge carriers is maintained by the surface electric field that defines the inversion layer. In other words, the inversion layer is to some extent electrically isolated from the n-type bulk by a depletion region (see Fig. 8). As we discuss below, the inversion layer revealed by our Hall measurements is likely the main reason that pyrite has a photovoltage much smaller than its band gap permits.

Critical additional evidence for surface conduction in an inversion layer comes from the dependence of the Hall data on sample thickness. In principle, decreasing the slab thickness should decrease the ratio of the bulk to surface layer thicknesses and change $\sigma$ and $R_H$ according to eqn (10) and (11) in the Experimental section. Only when surface conductivity is quite different from bulk conductivity do we expect to affect the Hall data by changing the surface-to-volume ratio. We acquired Hall data on several pyrite slabs as a function of thickness by using mechanical polishing to progressively thin the slabs between measurements. Care was taken to prepare the surfaces in the same way for each measurement in order to avoid uncontrolled differences in surface morphology or chemistry that might influence the results. Fig. 5 presents Hall data (80–350 K) for a representative crystal at thicknesses of 820, 490, 140, and 60 μm, along with predictions from the model (dashed traces). We observe systematic changes in the low-temperature data that are in qualitative agreement with predictions from the multi-layer model. With decreasing sample thickness, the $|R_H|$ maximum shifts to higher temperatures (from 118 to 152 K in Fig. 5) and the low-temperature $\sigma$ increases by a factor of ~20 with no change in activation energy. The $R_H$ sign reversal also occurs at progressively higher temperatures (from 85 to 100 K). These effects are geometric: since surface layer conductance is a larger fraction of the total conductance in thinner samples, surface conduction starts to dominate $R_H$ at higher temperatures as the crystal is thinned. Because the surface conductivity is much larger than bulk conductivity at low temperatures (for example, $\sigma_{bulk} = 6 \times 10^{-7}$ S cm$^{-1}$ and $\sigma_{surf} = 0.53$ S cm$^{-1}$ at 100 K), the total sample conductivity increases for thinner samples. We note that the systematic thickness dependence of $|R_H|$ and $\sigma$ in Fig. 5 is in itself sufficient evidence to prove that pyrite has a conductive surface layer. As expected, control experiments on silicon single crystals showed no change in $|R_H|$ or $\sigma$ as a function of slab thickness because silicon lacks a conductive surface layer (Fig. S18†).

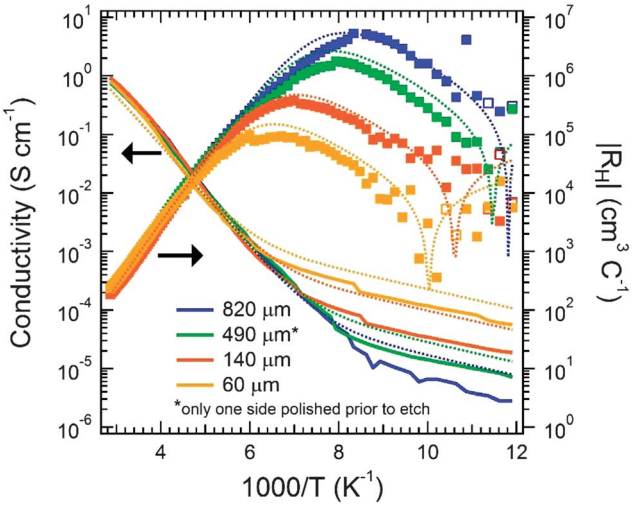


Fig. 5 Dependence of Hall data on sample thickness. The crystal was polished on both sides and etched in piranha solution for 2 minutes prior to each measurement (except for the 490 μm data, for which only one side was freshly polished prior to piranha treatment). Dotted curves are predictions (not fits) from the multi-layer model using the sample thickness and parabolic DOS($E$) functions.

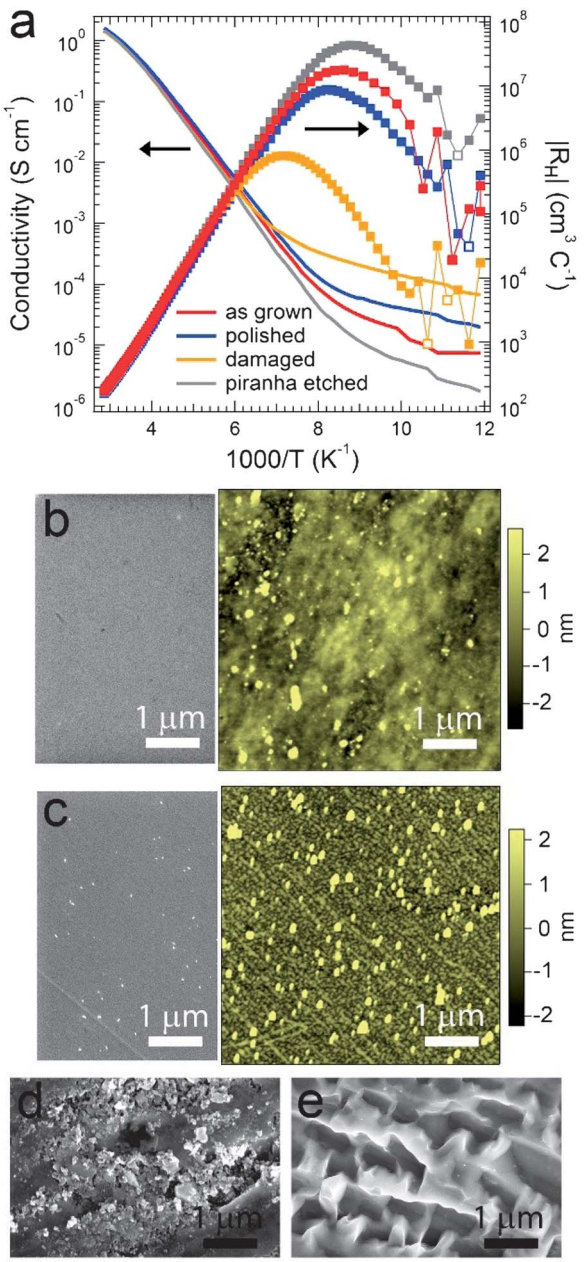


Fig. 6 Dependence of the Hall data on gross surface modifications. (a) Data for one pyrite sample after the following sequence of surface treatments: as grown = no treatment of top surface, bottom surface rough cut with a diamond saw; polished = after polishing both sides to ~2 nm RMS roughness (see Experimental); damaged = after aggressive grinding of both sides with SiC paper; piranha etched = after a 5 min etch in piranha solution. Sample thickness: 400–500 μm. (b) SEM and AFM images of the as-grown crystal. RMS roughness = 1.3 nm. (c) SEM and AFM images of the polished crystal. Roughness = 1.6 nm RMS. The particles present in (b) and (c) were determined to be pyrite by energy dispersive spectroscopy. (d) SEM image of the crystal after damaging the surface with SiC grinding paper. (e) SEM image of the crystal after etching in piranha. Note that while a 5 min piranha etch of a damaged crystal results in pitting, the same etch of a polished crystal leaves an unpitted, planar surface. See Fig. S20† for SEM and AFM images of a polished, piranha-etched sample and Fig. S21† for SEM images used to determine the etch rate of the pyrite crystals in piranha solution.

The low-temperature Hall data is also sensitive to mechanical and chemical modification of the crystal surface, as expected if surface conduction dominates transport. Fig. 6 shows how $|R_H|$ and $\sigma$ change as a typical pyrite slab is cut, polished, damaged by grinding with SiC paper, and then etched in piranha solution to remove the surface damage. Polishing the as-grown slab causes a small increase in conductivity and slight shift of the $|R_H|$ maximum to higher temperature. Damaging the surface by mechanical grinding results in a much larger change of the same kind, consistent with a thicker and/or more conductive surface layer. Rocking curves show that significant lattice disorder is induced by the grinding step (Fig. S19†). A brief piranha or nitric acid etch removes this surface damage, dramatically lowers the conductivity, and shifts the $|R_H|$ maximum to lower temperature (from 140 to 114 K), indicating a decrease in the thickness and/or conductivity of the surface layer to below that of the polished crystals. Modeling shows that the effective surface acceptor density decreases by a factor of ~15 after piranha or nitric acid etching of polished crystals. These surface modifications have a large impact on the low-temperature data (where the surface layer dominates transport), but little impact on either $\sigma$ or $R_H$ at temperatures above ~160 K. A chemical understanding of these changes is the goal of ongoing studies. It is possible that piranha and nitric acid treatments reduce the conductivity/thickness of the surface layer by oxidizing the surface and passivating some fraction of the surface states. The partial suppression of surface conduction by oxidizing etches raises the hope that suitable chemical treatments can be devised to control and eliminate the inversion layer at the pyrite surface.

We used ultraviolet photoelectron spectroscopy (UPS) to independently confirm the existence of the inversion layer (see Experimental). Fig. 7 shows room-temperature He I UP spectra of a polished pyrite (111) slab acquired before and after cleaning the surface with a sequence of UV/ozone (UVO) and ammonium fluoride treatments to remove adventitious organic and oxide contamination. Both spectra show that the Fermi level lies 0.11 ± 0.05 eV above the valence band maximum (inset Fig. 7), *i.e.*, the surface is p-type in both cases assuming that the surface band gap is greater than ~0.2 eV. In light of the Hall results presented above, it follows that the surface must feature an inversion layer with a band diagram similar to Fig. 8 (if the surface and bulk band gaps are the same) or Fig. S22† (if the surface band gap is smaller than the bulk band gap; see below). The UPS data contain significant information in addition to the position of the surface Fermi level, but a more detailed analysis of the surface preparation procedures and UPS results is beyond the scope of this paper and will be published elsewhere.[35]

The likely existence of an inversion layer at the surface of pyrite was established twenty years ago by Bronold and co-workers using UPS measurements of vacuum-cleaved (100) single crystals.[10,36,37] Our UPS results reproduce this early work and, together with our Hall analysis, show that it is correct for pyrite (111), (210), and (100) surfaces. Following Bronold, we attribute the pinned Fermi level and resulting inversion layer to intrinsic surface states with energies near the valence band edge. The inversion layer probably originates from a symmetry

 

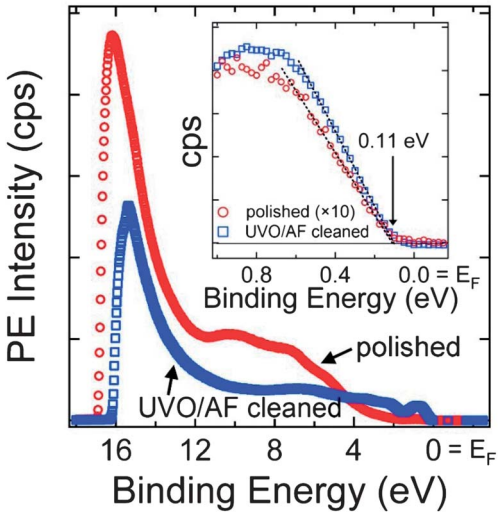


Fig. 7 Upper valence band spectra of a polished pyrite (111) slab before and after surface cleaning by UV/ozone and aqueous $NH_4F$ etching. Inset is a magnified view of the edge of the valence band. In both cases, $E_F - E_V \approx 0.11$ eV and the surface of the n-type crystal is p-type.

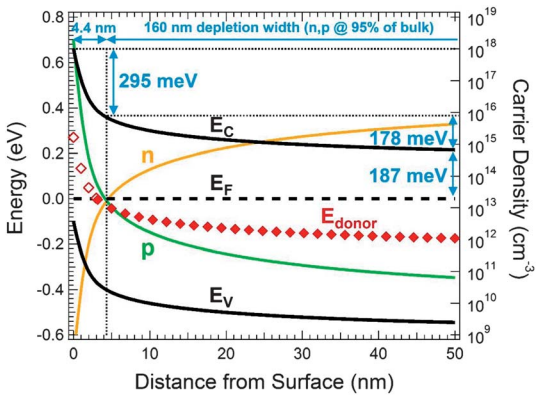


Fig. 8 Calculated equilibrium band diagram of the pyrite surface at 300 K (see Experimental) assuming $E_g = 0.76$ eV (see Section 2.3) and zero compensation. In the bulk, $E_F$ is located ~190 meV below the conduction band edge (consistent with $N_D = 6 \times 10^{18}$ cm$^{-3}$ and $E_C - E_D = 390$ meV from Hall data). At the surface, $E_F$ is pinned ~100 meV from the valence band edge (consistent with UPS data). Equilibration of bulk with surface results in steep upward surface band bending of ~480 meV and the generation of an inversion layer ($p > n$) approximately 4.4 nm thick (denoted by the vertical dotted line). The inversion layer is separated from bulk by a depletion layer approximately 160 nm thick (defined here as $n = 0.95n_{bulk}$). Most donors in the inversion layer are ionized (open red diamonds), which augments the surface electric field and results in a narrow triangular potential barrier across which carriers can readily tunnel. Tunneling is a loss mechanism that degrades the ability of the barrier to separate charge and produce voltage. As drawn, the top ~295 mV of the barrier is lost to tunneling, leaving a maximum photovoltage of only ~178 mV for any pyrite junction. The maximum $V_{OC}$ becomes ~340 mV if $E_g$ is assumed to be 0.94 eV rather than 0.76 eV. Fig. S22† shows a similar diagram for the case of a narrow band gap surface layer. Including bulk compensation in the calculation did not change the qualitative features of the diagram.

reduction at the pyrite surface and not from contamination (*e.g.*, oxide or adsorbed organic species). Experimental evidence for the inversion layer has been overlooked in recent efforts to explain the low voltage of pyrite photocells,[4,38] yet surface conduction in accumulation or inversion layers is quite common for semiconductors, with important examples including $Mg_2Sn$,[39] Ge,[40] HgCdTe,[41] pyrite $NiS_2$,[42] and InN.[43,44] It has taken until now to demonstrate the importance of surface conduction in pyrite for two reasons: first, many pyrite samples are too impure to clearly see surface conduction in Hall data and, second, the few examples of unusual Hall data reported in the literature went unnoticed or were interpreted as hopping.[28]

The inversion layer can account for the low photovoltage of pyrite photocells.[13] As originally argued by Bronold, the low voltage may be caused by thermionic field emission[45] through a thin triangular potential barrier at the surface of the crystal (Fig. 8).[10] At the pyrite surface, the iron coordination number is reduced from six to five. This symmetry reduction (distorted octahedral to square pyramidal coordination) creates iron-based surface states at energies close to the valence band edge. Fermi level equilibration of the n-type bulk with these surface states generates strong upward band bending and an inversion layer. During equilibration, donors near the surface rise above the Fermi level and are ionized, which augments the surface field and creates a thin triangular potential barrier through which majority carriers can tunnel directly or with the assistance of empty donors (Fig. 8). Because this leaky potential barrier is poor at separating charge, the dark current is large and the maximum $V_{OC}$ limited to ~0.2 V (*i.e.*, the portion of the barrier not shorted by tunneling). In this picture, increasing the $V_{OC}$ will require reducing the concentration of surface states (responsible for the inversion layer) as well as near-surface donors (responsible for the triangular tunnel barrier and, ultimately, the low $V_{OC}$). We estimate that reducing $N_D$ below ~$10^{17}$ cm$^{-3}$ would render field emission insignificant and boost the maximum $V_{OC}$ above 450 mV. However, our efforts to lower $N_D$ below ~$10^{19}$ cm$^{-3}$ have been unsuccessful so far and it remains to be seen whether these donors – which we believe are sulfur vacancies and associated defect clusters – are inevitable in pyrite.

The inversion layer can also explain why most polycrystalline pyrite thin films show the same electrical properties – a high hole concentration, low mobility (≤1 cm$^2$ V$^{-1}$ s$^{-1}$), and activated transport with a small activation energy of ~25 meV – regardless of preparation method.[11,13,46] Thin films are often dominated by surface effects due to their large surface-to-volume ratios. In the case of pyrite films, transport may be governed by surface conduction *via* the hole-rich accumulation/inversion layer around each crystallite. These surface layers would form continuous networks for long-range transport through the films. Unlike pyrite single crystals, which are dominated by surface conduction only at temperatures low enough to freeze out a sufficient fraction of the bulk electrons, pyrite thin films have a large surface volume fraction and are therefore dominated by surface conduction at all temperatures. The fact that pyrite films have the same activation energy (~25 meV) and low hole mobility (≤1 cm$^2$ V$^{-1}$ s$^{-1}$) as single

crystals in the low-temperature, surface conduction regime is strong evidence that the commonly-observed p-type electrical behavior of pyrite films is caused by conduction within a hole-rich surface layer.

Our Hall data can also be understood in terms of an inverted surface layer with a band gap that is smaller than the bulk band gap of pyrite. Several DFT studies have concluded that the low photovoltage of pyrite devices may be caused by narrowing of the "band gap" of the first three atomic layers of the pyrite surface (~0.7 nm) to less than 0.6 eV by intrinsic surface states or surface nonstoichiometry.[4,12] Very recently, Herbert *et al.* presented scanning tunneling spectroscopy (STS) evidence that the clean pyrite (100) surface has a band gap of 0.4 ± 0.1 eV.[47] We find that a thin surface layer with a reduced band gap ($E_g$ = 0.3–0.6 eV) has very similar electrical consequences to an inversion layer with the same band gap as bulk pyrite, namely: (i) both layers are p-type (since $E_F - E_V \approx 0.1$ eV at the surface) and responsible for the surface hole conduction we observe at low temperatures; (ii) both layers can restrict the $V_{OC}$ to ≤200 mV, albeit by different mechanisms (compare the band diagrams in Fig. S22† and 8: an inherently small built-in potential would cause the low $V_{OC}$ in the former case, while thermionic field emission in responsible in the latter case); (iii) the two layers have the same origin (intrinsic surface states) and so the same remedy (passivation of surface states and near-surface defects). Changing the band gap of the surface layer has a negligible effect on our Hall modeling, meaning that we cannot tell whether the band gap of the surface differs from that of the bulk on the basis of the Hall data alone. Likewise, UPS probes <1 nm into the crystal surface and the data in Fig. 7 are consistent with any value of the surface gap greater than 0.2–0.3 eV. A combined UPS and inverse photoemission study could complement STS to definitively establish the band gap of the pyrite inversion layer.

### 2.3. Assessment of the bulk band gap of pyrite

In Section 2.2, we presented evidence for an inversion layer at the surface of n-type pyrite single crystals and argued that thermionic field emission across this inversion layer is likely responsible for the low photovoltage of pyrite photocells, in line with earlier work by Bronold *et al.*[10] Our data are also consistent with the presence of a narrow-gap surface layer that generates only a small potential barrier and thus a small maximum $V_{OC}$. In Section 2.3, we evaluate an important alternative explanation for the low $V_{OC}$ of pyrite, namely that the bulk band gap of pyrite has been overestimated in literature and is actually substantially smaller than ~0.95 eV at room temperature. If the bulk electronic band gap was in fact 0.5–0.6 eV, then the maximum $V_{OC}$ might be 0.2–0.3 eV, in good agreement with experiment. Indeed, a small band gap is a more parsimonious explanation for the low $V_{OC}$ than a leaky inversion layer. It is therefore important to reassess the size of the pyrite band gap as rigorously as possible.

The main reason to suspect that pyrite may have a smaller band gap than commonly believed is a series of density functional theory (DFT) studies[4,22,38] showing that the conduction band of pyrite features a long tail of states extending to the edge of the gap (see Fig. S10†). Because of its low density of states (DOS) and small optical matrix elements,[31] this tail could easily be invisible to the typical spectroscopic measurements used to estimate semiconductor band gaps, leading to systematic overestimation of the pyrite gap when measured optically. To the best of our knowledge, there is no convincing experimental evidence for this tail of states. Maps of the conduction band DOS by inverse photoemission spectroscopy[48,49] and electron energy loss spectroscopy[50] lack a clear tail, but this may simply reflect the inherent difficulty of detecting a weak DOS tail and the fact that searching for a tail was not a focus of these earlier studies. Experiments designed to detect and characterize this proposed tail of states are necessary.

For materials with soft band edges, electrical measurements can provide more accurate band gap estimates than optical measurements. The electronic band gap is commonly extracted from the temperature-dependent conductivity in the intrinsic region using $\sigma(T) = A \exp\left(\frac{-E_g}{2kT}\right)$, with both $A$ and $E_g$ treated as independent of temperature.[45] However, this expression is based on several simplifications, including the parabolic band approximation, the free electron approximation, and the Boltzmann approximation, each of which may be inappropriate for pyrite. DFT results show that the valence and conduction bands of pyrite are not parabolic and the DOS($E$) functions are neither free carrier like nor symmetric (the valence band has a much larger DOS than the conduction band). Violation of the parabolic band approximation by pyrite has been previously pointed out by Ferrer *et al.*[51,52] If the DOS from DFT is correct, then the Fermi level must lie close to the conduction band edge at high temperatures (see Fig. S12†), and the slope of an Arrhenius conductivity plot will not correspond to half of the band gap. This complicates any estimate of the pyrite band gap from the intrinsic conductivity.

A further complication is that both $A$ and $E_g$ depend on temperature. In deriving the normal expression for $\sigma(T)$, the DOS is approximated with the free electron gas and Boltzmann statistics are used to give $n_i(T) = \sqrt{N_V(T)N_C(T)}\exp\left(\frac{-E_g}{2kT}\right) \propto T^{3/2}\exp\left(\frac{-E_g}{2kT}\right)$. Combining this expression with the temperature-dependent mobility due to phonon scattering ($\mu(T) \propto T^{-3/2}$) yields the usual $\sigma(T)$ equation with constant $A$. This equation is probably not correct for pyrite for the reasons mentioned above, and $A$ may change significantly with temperature depending on the explicit forms of DOS($E$) and $\mu(T)$. Furthermore, $E_g$ typically varies with temperature according to the empirical relation $E_g = E_{g_0} - \frac{aT^2}{T+b}$, resulting in a substantial change in $E_g$ (often several hundred meV) from room temperature to within the intrinsic region. A numerical model using explicit forms of DOS($E$) and $E_g(T)$ and good estimates for $\mu(T)$ is therefore required to determine the pyrite band gap from $\sigma(T)$ data. This is the approach we adopt in the following analysis.

Arrhenius conductivity plots of three pyrite crystals (300–750 K) are shown in Fig. 9a. Since the pyrite samples were measured at high temperature in nitrogen or vacuum ambient

 

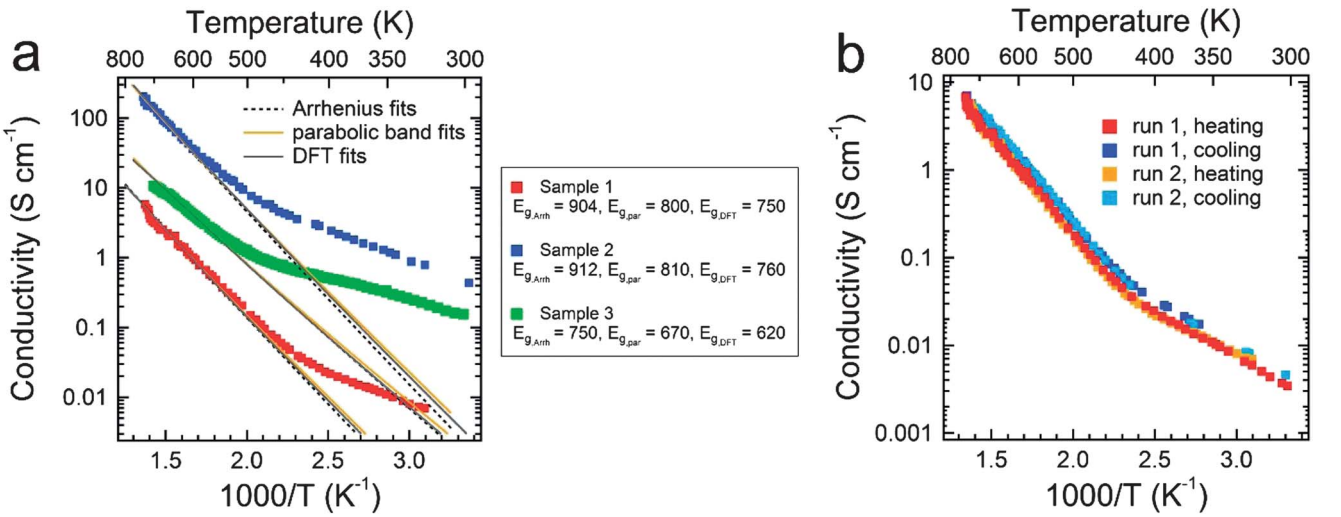


Fig. 9 Conductivity of pyrite crystals in the intrinsic region. (a) High-temperature conductivity data for three crystals. The intrinsic region of each sample is fit with the simple Arrhenius expression (dotted lines) as well as models employing DFT or parabolic DOS($E$) values (gray and yellow lines, respectively). All fits assume $\mu(T) \propto T^{-2.5}$. Listed to the right of the graph are room-temperature $E_g$ values (in meV) determined by the three different approaches. (b) Two sets of heating and cooling curves (300 K to 750 K) for Sample 1. The activation energy is unchanged by heating, suggesting that surface sulfur loss and possible phase transitions from $FeS_2$ to sulfur-deficient $Fe_xS_y$ and FeS do not appreciably alter the electrical properties of the samples. Heating and cooling rates = 7–14 °C min$^{-1}$. Sample thickness = 700–1040 μm.

(see Experimental), we first checked whether sulfur loss and the formation of sulfur-deficient phases at the crystal surface may affect the conductivity data. Fig. 9b shows that the $\sigma(T)$ curves of sample 1 are unchanged over several cycles of heating and cooling, suggesting that loss of surface sulfur has negligible impact on the data. *In situ* XRD scans of crystals subjected to these heat treatments confirmed that the formation of sulfur-deficient phases (FeS and $Fe_7S_8$) becomes appreciable only above 775 K (Fig. S23†) or after prolonged heat soaking at somewhat lower temperatures (>675 K). Furthermore, our multi-layer model shows that the buildup of a metallic surface layer of any significant thickness would produce an obvious upward shift in the conductivity curves, which is not observed. We therefore believe that the $\sigma(T)$ data in Fig. 9 reflect the behavior of pyrite itself in the intrinsic region.

Prior to analyzing the $\sigma(T)$ data, we also estimated whether thermal excitation of electrons at intrinsic temperatures could fill enough of the conduction band tail of states to result in a Burstein–Moss type increase of the apparent electronic band gap. However, the intrinsic electron density at even the highest temperatures explored here (~750 K) is still several orders of magnitude smaller than the integrated DFT DOS at the edge of the conduction band (Fig. S24†). Therefore, the DOS in the tail is much too large to cause a significant Burstein–Moss shift in the intrinsic region, and we estimate that any increase in apparent band gap due to state filling is less than 25 meV. This further confirms that the $\sigma(T)$ data in Fig. 9 can be related to the room-temperature electronic band gap of pyrite.

We calculated room-temperature band gaps from the $\sigma(T)$ data using three different approaches. The first approach assumes the naive relation $\sigma(T) = A \exp\left(\frac{-E_g}{2kT}\right)$ with a temperature-independent $E_g$. Simple Arrhenius fits to the intrinsic region yield band gaps of 904, 912, and 750 meV for the three samples in Fig. 9, in good agreement with previous results using this approach.[53] In the other two approaches we employed our numerical model to iteratively fit the intrinsic $\sigma(T)$ data to determine $E_g$ at high temperature and then extrapolated this value to room temperature using a measured $E_g(T)$ curve for pyrite (see below). Modeling the data with the DFT DOS gives room-temperature band gaps of 750, 760, and 620 meV, while using the parabolic DOS instead of the DFT DOS results in gaps of 800, 810, and 670 meV. The band gap values are ~50 meV smaller for the DFT DOS because the larger asymmetry between the valence and conduction band DOS shifts the Fermi level upwards and requires a smaller calculated band gap to yield a given slope in the $\sigma(T)$ data (see Fig. S12†). The same effect also results in a higher calculated carrier density, which requires an unrealistically low electron mobility to fit the data with the DFT DOS. Since the parabolic DOS provides a significantly better description of the pyrite Hall data than the DFT DOS, we conclude that the larger band gaps are more accurate. However, the accessible temperature range of the intrinsic region is fairly small (constrained at the low end by doping and the high end by sulfur loss). This causes some insensitivity to the fit parameters and an error of ±50 meV in the band gap estimates. We also note a striking sample-to-sample variation in $E_g$ of ~200 meV across the seven samples we measured (see Fig. S25†). This variation may result from larger band tails in lower quality samples. Using the three highest $E_g$ values in our data set and the $E_g(T)$ relationship described in the next paragraph, we conclude that the room-temperature electronic band gap of high-quality pyrite crystals is 0.80 ± 0.05 eV. The average $E_g$ of the three samples in Fig. 9 – which includes one crystal with a particularly small estimated band gap – is 0.76 eV, within the specified range.

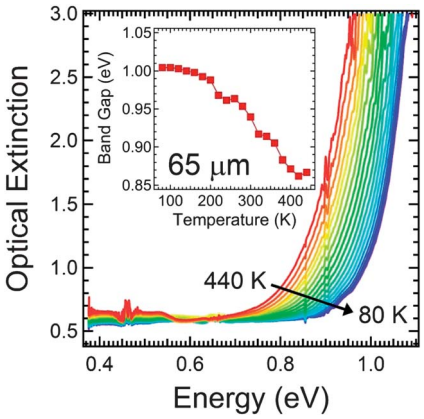


Fig. 10 Optical extinction spectra of a 65 μm thick pyrite crystal as a function of temperature (80–440 K). Inset is a plot of $E_g$ *versus* temperature as determined by linear extrapolation of the absorption coefficient data after correcting for dispersion of the refractive index. If Tauc plots are used instead, $E_g$ is about 50 mV higher (lower) for the direct (indirect) Tauc plot, while the temperature dependence of $E_g$ is unaffected. See Fig. S26† for a comparison of these data with similar data on silicon.

The temperature dependence of $E_g$ was determined by measuring the *optical* gap of thin polished pyrite crystals from 80 to 440 K using transmission spectroscopy. Fig. 10 shows the raw extinction spectra as well as the optical gap extracted by linear extrapolation of the absorption coefficient curve to its intersection with the *x*-axis. Tauc plots – which presume parabolic bands – give the same $E_g(T)$ values to within 50 meV. We find that the optical gap decreases from 1.00 eV at 80 K to 0.94 eV at 300 K and 0.86 eV at 440 K (the highest temperature possible with our equipment). Our $E_g(T)$ curve is in good agreement with several previous reports,[54,55] particularly the work of Karguppikar and Vedeshwar[56] (see Fig. S25† for a compilation of literature data on the pyrite gap). Although the magnitude of $E_g$ may be overestimated by this optical method (as discussed above), the temperature dependence of $E_g$ should be reliable, and we use the $E_g(T)$ curve of ref. 56 to extrapolate the modeled high-temperature electronic gaps to 300 K. Based on this analysis, we find that the most probable electronic band gap of pyrite is 0.80 ± 0.05 eV at room temperature, as mentioned above. Although this value is somewhat smaller than the optical gap (0.94 eV), it is still large enough to support a photovoltage of 450–500 mV in pyrite photocells. We conclude that the pyrite photovoltage is not limited to ~200 mV by a small bulk band gap.

# 3. Conclusions

High-quality, ultrapure iron pyrite single crystals have been grown in sodium polysulfide flux. Hall effect measurements of these crystals show an unusual minimum and sign change of the Hall coefficient at ~120 K and ~80 K, respectively. Numerical fitting of the Hall data using a multi-layer transport model that includes a self-consistent Fermi level reveals the existence of a hole-rich inversion layer at the surface of the n-type crystals. This inversion layer is a channel for the surface conduction of holes in pyrite. Electrons in the crystal bulk are frozen out at low temperatures to the extent that the holes in the inversion layer dominate conduction. The presence of the hole inversion layer is corroborated by UPS measurements showing $E_F - E_V \approx 0.1$ eV as well as Hall effect experiments as a function of crystal thickness and physicochemical modification of the crystal surface. The inversion layer can explain both the low photovoltage of pyrite photocells (caused by tunneling across part of the inversion layer) and the common high p-type conductivity of polycrystalline pyrite thin films (caused by the dominance of surface conduction in these high surface-to-volume ratio samples). Our data can also be understood in terms of a surface layer with a reduced band gap, with the $V_{OC}$ in this case limited by weak band bending rather than tunneling. Transport within the surface layer may occur by hopping at low temperature, but more data are needed to confirm this possibility.

We also used our single crystals to assess whether the bulk band gap of pyrite is significantly smaller than the widely accepted value of ~0.95 eV at room temperature. Our optical measurements yield a band gap of 0.94 eV, in agreement with literature (as expected), while modeling of the intrinsic electrical conductivity using two different DOS functions results in a somewhat lower best-fit value of 0.80 ± 0.05 eV. Given the assumptions involved in calculating the pyrite band gap from conductivity data, we conclude only that the electronic gap of high-quality pyrite is probably ~0.80 eV, which is large enough to support a photovoltage of ~500 mV from pyrite photocells under normal sunlight. In our view, all of the experimental evidence available supports the hypothesis that the low $V_{OC}$ of pyrite is caused by a surface layer, not a small bulk band gap.

This study confirms that pyrite suffers from a strong inversion layer that likely limits the useful built-in voltage of pyrite junctions to ~200 mV, but the next question is whether this conductive surface layer can be fixed. Fixing pyrite will depend on passivating the surface states that cause the surface layer and lowering the concentration of near-surface donors (probably sulfur vacancies) that promote tunneling across it. Etching polished crystals in piranha reduces the effective surface acceptor density by a factor of ~15, but more rational and controlled surface treatments should give better results. We have shown that flux-grown single crystals can provide new insights to fundamental questions about pyrite. Moving forward, such crystals will serve as an important platform for determining whether surface passivation can be used to produce high $V_{OC}$ photovoltaic junctions from pyrite.

# 4. Experimental

## 4.1. Materials

We used starting materials of the highest available purity (metals basis) and further purified each to remove possible nonmetal impurities such as water and oxygen. Iron powder (99.998%, 22 mesh, Alfa Aesar) was loaded into a pyrolytic boron nitride (pBN) crucible and reduced in a quartz tube furnace in a flow of 5% $H_2$/95% Ar at 300 °C for 15 hours to remove water and surface oxides. Higher temperatures (>450 °C) led to

 

undesirable agglomeration of the iron powder. Sulfur powder (99.9995%, Alfa Aesar) was degassed and dried in a quartz flask under a dynamic vacuum of ~30 mTorr at 130 °C for 3 hours. $Na_2S \cdot 9H_2O$ (>99.99%, Aldrich) was crushed, then dried and degassed in a quartz flask under a dynamic ~30 mTorr vacuum at 300 °C for 5 hours, resulting in a mixture of fine colorless and yellow powder ($Na_2S$ and polysulfides, respectively). After purification, all three starting materials were immediately transferred to an $N_2$-filled glovebox (<0.1 ppm $O_2$, LC Technologies) without exposure to air.

### 4.2. Flux growth of single crystals

Pyrite crystals were grown in alumina crucibles (99.5%, LSP Ceramics) or pBN crucibles (99.999%, Morgan Technical Ceramics) sealed in evacuated quartz ampoules. All procedures were performed rigorously air free. 0.50 grams of iron (8.9 mmol) was placed in the bottom of the crucible, followed by 0.71 grams of $Na_2S$ (9.1 mmol) and 1.29 grams of sulfur (40.2 mmol). The crucible was then loaded in a quartz tube and the tube was connected to a vacuum hose with a closed isolation valve. This apparatus was removed from the glovebox, attached to a vacuum manifold, purged with 99.999% Ar, pump/purged to <20 mTorr three times, and sealed at <20 mTorr with a hydrogen/oxygen torch. The quartz ampoule was held vertically the entire time to avoid mixing or spilling the contents of the crucible. The ampoule was placed in the center of a vertical tube furnace, heated at a rate of 13 °C $min^{-1}$ to 780 °C, held at 780 °C for 6 hours, cooled to 625 °C over 24 hours, and finally cooled naturally to room temperature over 5 hours (36 hours total). The crucible was then removed from the ampoule and placed in a beaker of Millipore water for several hours to dissolve the flux. 80% of the time this procedure results in one large pyrite crystal, while several smaller crystals are produced 20% of the time. The crystals are sonicated in Millipore water to remove flux residue, rinsed many times with Millipore water, dried, and stored in the glovebox.

### 4.3. Crystal sectioning and surface preparation

Single crystals were mounted in epoxy (Buehler EpoxyCure) for sectioning. A slow-speed diamond saw (Model 650, South Bay Technology) was used to cut 500–1000 μm thick slabs from the flux crystals parallel to their largest surface facet (usually a {111} plane). The slabs were then released from the epoxy by soaking in dichloromethane for 2 hours. To obtain fine-polished surfaces with ~2 nm RMS roughness, as-cut slabs were first polished sequentially with SiC paper of grit size 600, 800, and 1000, followed by sequential lapping with 3 μm and 1 μm diamond slurries and, finally, 20 minutes of lapping with 50 nm $Al_2O_3$ slurry (Buehler MasterPrep). Residual slurry particles were removed by sonication in Millipore water. The polished slabs were then transferred to the glovebox for Hall effect measurements. Note that some slabs were measured without any polishing (*i.e.*, as-grown surfaces) or without the final $Al_2O_3$ slurry polish (as indicated in the text).

Etching was carried out using freshly prepared piranha solution (3 : 1 concentrated $H_2SO_4$ to 30% $H_2O_2$). Unless otherwise noted, samples were immersed in piranha for 2 minutes and then rinsed with deionized water and methanol and blown dry.

A p-type silicon (100) wafer (B doped, 500 μm, MTI Corp.) was used for Hall effect control experiments. For thickness studies, pieces of the wafer were ground on both sides with 800 grit SiC paper and measured with or without subsequent polishing of both sides with 1000 grit paper followed by diamond slurries. Ohmic contacts were made by scratching the corners of the sample with a diamond scribe, applying In/Ga eutectic to the scratched area and heating for 5 min at 80 °C. Silver paint was then applied on top of the eutectic.

### 4.4. Structural, elemental, and electrical characterization

Structure determination by single crystal X-ray diffraction was performed on a Bruker SMART APEX II diffractometer at 143 K using ~0.2 mm specimens removed from as-grown crystals. Diffraction data were collected on a CCD area detector using Mo Kα radiation ($\lambda = 0.71073$ Å). A full sphere of data was collected for each crystal. The APEX2 software package was used for data collection and determination of unit cell parameters.[57] Data were absorption corrected using SADABS-2008/1. The structures were solved by direct methods and refined by a full-matrix least-squares routine on $F^2$ with SHELXL97.[58] The diffraction symmetry was $m3$ and the systematic absences were consistent with the cubic space group $Pa\bar{3}$. Thin film X-ray diffraction (including room-temperature rocking curves, $2\theta$–$\omega$ scans, and pole figures) was performed on a Rigaku SmartLab diffractometer. X-ray rocking curves and $2\theta$–ω scans were acquired on the SmartLab configured with a Ge(440) × 4 monochromator featuring an angular resolution of 5.4 arcseconds. Synchrotron XRD measurements were performed on pulverized crystals in capillary transmission mode at Beamline 11-BM of the Advanced Photon Source ($\lambda = 0.413141$ Å) at Argonne National Laboratory. X-ray tomography measurements were performed on a Zeiss Xradia 410 Versa with a 4× objective lens. Raman spectroscopy utilized a Renishaw inVia confocal Raman microscope with a 50× objective lens and a 523 nm laser operating at less than 5 mW. Samples were measured in air. Scanning electron microscope (SEM) images were acquired on an FEI Magellan 400 XHR SEM. Surface topography was measured using an Asylum MFP-3D atomic force microscope (AFM). Optical transmission spectra were acquired on a PerkinElmer Lambda 950 spectrophotometer equipped with a Janis ST-100 cryostat. Helium pycnometry was carried out on a micro-Ultrapyc 1200e (Quantachrome Instruments).

Elemental composition of the crystals was determined by Evans Analytical Group using glow discharge mass spectrometry (GDMS), instrumental gas analysis (IGA), inductively coupled plasma optical emission spectroscopy (ICP-OES), and secondary ion mass spectrometry (SIMS). GDMS measurements were performed on a VG 9000 GDMS instrument (Thermo Scientific). Powdered pyrite specimens were pressed into high-purity In foil (99.99999%) previously cleaned with acid to remove surface impurities. Impurities in the In foil were analyzed prior to elemental analysis of each sample. Glow

discharge conditions of 1.0 kV, 2.0 mA, and 100 Pa of 99.9999% Ar were used for all measurements. Samples were pre-sputtered for five minutes prior to data acquisition. The intensities of the ion beams were measured with a Faraday cup for iron, sulfur and indium isotopes and a Daly conversion detector for all analytes in the samples. The efficiency of the detectors was calibrated using $^{180}$Ta (relative isotopic abundance of 0.012%) measured on the Daly detector and $^{181}$Ta (relative isotopic abundance of 99.99%) measured on the Faraday cup during analysis of pure Ta metal. Scan points per peak were 70 channels, DAC steps of 7 with integration times of 100 and 160 ms for the Daly detector and Faraday cup, respectively. IGA measurements were performed on a Leco TC 600 oxygen/nitrogen analyzer, a Horiba EMIA-820V carbon/sulfur analyzer, and a Horiba EMGA-621W hydrogen analyzer. Samples were prepared in a glovebox by loading small crystal pieces into Sn capsules for the inert gas fusion measurements. ICP-OES measurements used a PerkinElmer Optima 7300V spectrometer operating at 1300 W. 0.1 g samples were digested in a closed vessel containing 2 mL $HNO_3$ and 6 mL HCl in 5 mL $H_2O$ in an Anton Paar multiwave 3000 microwave (HF100 rotor).

Secondary ion mass spectrometry (SIMS) was performed on a PerkinElmer Physical Electronics Model 6600 dynamic SIMS instrument using 4 keV Cs ions for anions (S, O, H, C, F, and Cl) and 5 keV $O_2$ ions for cations (Na, K, Mg, Ca, Cr, and Al). Estimated detection limits were $1 \times 10^{15}$ atoms cm$^{-3}$ for Na, K, Al, Mg, Cr, and Ca, $5 \times 10^{17}$ atoms cm$^{-3}$ for C, $2 \times 10^{18}$ atoms cm$^{-3}$ for O and H, and $5 \times 10^{16}$ atoms cm$^{-3}$ for F and Cl. Atomic concentrations are accurate to within a factor of two for oxygen and a factor of five for all other elements. The depth scale was quantified by measuring the analysis craters with a stylus profilometer.

Angle-integrated UPS spectra were acquired using He I radiation in normal emission using a customized Physical Electronics Model 5600 photoelectron spectroscopy system that has been described previously.[59] Data were taken at room temperature on "as-polished" crystals and after a chemical cleaning process[31] performed within the glovebox portion of the cluster tool to which the photoemission system is directly attached. Satellites due to non-monochromatic He I radiation were subtracted numerically. The binding energy scale of the spectrometer was calibrated using sputter-cleaned metal foils.

Hall effect data were acquired from 80 to 350 K on an Ecopia HMS-5000 instrument (0.55 T magnet) inside an $N_2$-filled glovebox using the van der Pauw method. Samples were mounted with thermal grease (Apiezon Type N) to a glass slide bonded to the sample stage. Ohmic contacts were made with colloidal silver paste. The Hall coefficient was calculated as $R_H = \frac{V_H d}{IB}$, where $V_H$ is the measured Hall voltage, $d$ the crystal thickness, $I$ the applied current, and $B$ the magnetic field strength. The applied current was adjusted from 200 nA at 80 K to 1–2 mA at 350 K. Hall effect data were also acquired at Lake Shore Cryotronics on a Model 9709A Hall Measurement System using a DC field strength of 2 T from 40–350 K and a 8404 AC/DC HMS using an AC field strength of 0.63 T RMS from 350–700 K. Ohmic contacts were made with colloidal silver paste. The applied current was adjusted from 50–100 nA at 40 K to 8–10 mA at 700 K. Representative plots of $R_H$ as a function of magnetic field are available in the Supporting Information (Fig. S27†). Conductivity values from the different measurement setups showed excellent agreement across the range of overlapping temperatures. Magnetoresistance measurements were performed in the 9709A system using a DC field strength of up to 90 kOe. The current at 300 K and 70 K was 10 mA and 100 nA, respectively. The resistivity at each magnetic field was calculated using the standard van der Pauw method.

Additional high-temperature conductivity data were obtained in a four point geometry by heating pyrite slabs with an as-grown top surface and as-cut bottom surface to 750 K on a hotplate inside an $N_2$-filled glovebox. The samples were heated rapidly (30–60 minutes) to minimize the loss of surface sulfur and conversion of the surface of the pyrite crystal to polycrystalline pyrrhotites ($Fe_xS_y$) and/or troilite (FeS). Data were recorded during both heating and cooling to check for thermal hysteresis due to this surface phase transition. In all cases, the cooling curve showed an unchanged slope and <20% higher conductivity. The applied current was adjusted from 1 mA at 300 K to 10–100 mA at 750 K to account for the change in sample conductivity.

### 4.5. Modeling of Hall data

Electrical conductivity and Hall coefficient data were modeled using the multilayer conduction model of Petritz.[34] Our implementation of the model assumes that electrical transport occurs in parallel through three layers – the crystal bulk and identical surface inversion layers on the top and bottom of the single-crystal slab – while neglecting currents across their interfaces. Calculation of the Fermi level ($E_F$), carrier concentrations ($n$ and $p$), conductivity ($\sigma$), and Hall coefficient ($R_H$) of the bulk and surface layers utilizes the charge neutrality condition:

$$N_D^{+} + p = N_A^{-} + n \tag{3}$$

where $N_D^{+}$ and $N_A^{-}$ are the concentrations of ionized donors and acceptors, given by[45]

$$N_D^{+} = \frac{N_D}{1 + \exp\left[\frac{(E_F(T) - E_D)}{(kT)}\right]} \tag{4}$$

$$N_A^{-} = \frac{N_A}{1 + \exp\left[\frac{(E_A - E_F(T))}{(kT)}\right]} \tag{5}$$

Here, $N_D$ and $N_A$ are the concentrations of donors and acceptors and $E_D$ and $E_A$ are their respective energy levels. The carrier concentrations are given by

$$n(T) = \int_{E_C}^{\infty} \mathrm{DOS}(E) \left( \frac{1}{e^{\left[\frac{E - E_F(T)}{kT}\right]} + 1} \right) dE \tag{6}$$

$$p(T) = \int_{-\infty}^{E_V} \mathrm{DOS}(E)\left(1 - \frac{1}{e^{\left[\frac{E-E_F(T)}{kT}\right]} + 1}\right)\mathrm{d}E \qquad (7)$$

Because the valence and conduction bands of pyrite are probably not parabolic, we compare in most calculations the parabolic DOS($E$) against an explicit numerical DOS($E$) obtained from our recent density functional theory (DFT) calculations of the pyrite band structure (see Fig. S11† for the two DOS($E$) plots).[22] In accord with literature and our own optical measurements (see text), we use a temperature-dependent band gap, $E_g(T) = E_g(0) - \frac{T^2 \times 0.00189\ \text{eV K}^{-1}}{T + 1915\ \text{K}}$, and assume equal shifting of the conduction and valence band edges with temperature.[54,56]

The calculation is performed by substituting eqn (4)–(7) into eqn (3) to give a self-consistent expression for $E_F(T)$ that is numerically solved for $E_F$ at each temperature. After calculating $n(T)$ and $p(T)$ from $E_F(T)$, the conductivity $\sigma(T)$ and Hall coefficient $R_H$(T) are obtained from the general expressions:

$$\sigma(T) = e(n\mu_e + p\mu_h) \qquad (8)$$

$$R_H(T) = \frac{E_y}{J_x B} = \frac{p\mu_h{}^2 - n\mu_e{}^2}{e(p\mu_h + n\mu_e)^2} \qquad (9)$$

where the temperature-dependent carrier mobilities $\mu_e$ and $\mu_h$ are extrapolated from unipolar regions of the Hall data (see ESI†). The electron mobility follows a $T^{-2.5}$ law at temperatures above ~150 K, as expected for phonon scattering. Finally, the contributions of the bulk and surface layers are combined to determine the total $\sigma$(T) and $R_H(T)$:[34]

$$\sigma_{total} = \sigma_b \frac{d_b}{d} + 2\sigma_s \frac{d_s}{d} \qquad (10)$$

$$R_{H,total} = R_{H,b}\left(\frac{\sigma_b}{\sigma_{total}}\right)^2 \frac{d_b}{d} + 2R_{H,s}\left(\frac{\sigma_s}{\sigma_{total}}\right)^2 \frac{d_s}{d} \qquad (11)$$

where $d_b$ and $d_s$ are the thicknesses of the bulk and the surface layers, respectively, and $d = d_b + 2d_s$ is the total slab thickness. Overall, there are five free parameters used for modeling the Hall data ($N_D$, $N_A$, $E_D$, $E_A$, and $\mu_h$) as well as four quantities parameterized from experimental data or theory (DOS($E$), $E_g(0)$, $\mu_e$, $d_s$). Some calculations also included compensation in the bulk by adding a bulk acceptor with concentration $N_{A,bulk}$ and ionization energy $E_A - E_V = 50$ meV. The calculation routine was implemented in Igor Pro 6.12.

### 4.6. Calculation of surface band diagrams

The software program 1D Poisson (http://www3.nd.edu/~demand/) by G. Snider was used to calculate band edge energies and carrier concentrations as a function of distance from the crystal surface (Fig. 8 and S22†). The inversion layer was modeled by assuming a Schottky barrier at the surface of n-type pyrite (with $N_D$ and $E_D$ taken from Hall effect results) with a barrier height chosen so that the Fermi level was located ~100 meV above the valence band edge, in agreement with UPS results.

## Conflict of interest disclosure

The authors declare no competing financial interest.

## Acknowledgements

We thank J. Tolentino for help with variable-temperature absorption spectroscopy and B. Mercado for single crystal XRD data. M. L. and M. L. acknowledge support from the U.S. Department of Energy under Contract No. DE-EE0005324, funded by the SunShot Next Generation Photovoltaics II (NextGen PVII) program. N. F. and N. B. were supported by the SOLAR program of the National Science Foundation (Award No. CHE-1035218). C. L. P. acknowledges support by the U.S. Department of Energy under Contract No. DE-AC36-08-GO28308 with the National Renewable Energy Laboratory. Use of the Advanced Photon Source at Argonne National Laboratory was supported by the U.S. Department of Energy, Office of Science, Office of Basic Energy Sciences, under Contract No. DE-AC02-06CH11357. We thank Z. Fisk for use of the quartz tube sealing setup and Quantachrome Instruments for pycnometry measurements. SEM and XRD work was performed at the Laboratory for Electron and X-ray Instrumentation (LEXI) at UC Irvine.

## References

1 A. Ennaoui, S. Fiechter, W. Jaegermann and H. Tributsch, *J. Electrochem. Soc.*, 1986, **133**, 97.
2 K. Büker, N. Alonso-Vante and H. Tributsch, *J. Appl. Phys.*, 1992, **72**, 5721.
3 A. Ennaoui, A. S. Fiechter, C. Pettenkofer, N. Alonso-Vante, K. Büker, M. Bronold, C. Höpfner and H. Tributsch, *Sol. Energy Mater. Sol. Cells*, 1993, **29**, 289.
4 L. P. Yu, S. Lany, R. Kykyneshi, V. Jieratum, R. Ravichandran, B. Pelatt, E. Altschul, H. A. S. Platt, J. F. Wager, D. A. Keszler and A. Zunger, *Adv. Energy Mater.*, 2011, **1**, 748.
5 C. Wadia, Y. Wu, S. Gul, S. K. Volkman, J. Guo and A. P. Alivisatos, *Chem. Mater.*, 2009, **21**, 2568.
6 N. Alonso-Vante, G. Chatzitheodorou, S. Fiechter, N. Mgoduka, I. Poulios and H. Tributsch, *Sol. Energy Mater.*, 1988, **18**, 9.
7 M. Birkholz, S. Fiechter, A. Hartmann and H. Tributsch, *Phys. Rev. B: Condens. Matter Mater. Phys.*, 1991, **43**, 11926.
8 R. Murphy and D. R. Strongin, *Surf. Sci. Rep.*, 2009, **64**, 1.
9 K. M. Rosso, U. Becker and M. F. Hochella, *Am. Mineral.*, 1999, **84**, 1535.
10 M. Bronold, C. Pettenkofer and W. Jaegermann, *J. Appl. Phys.*, 1994, **76**, 5800.
11 S. Seefeld, M. Limpinsel, Y. Liu, N. Farhi, Y. N. Zhang, N. Berry, Y. J. Kwon, C. L. Perkins, J. C. Hemminger, R. Q. Wu and M. Law, *J. Am. Chem. Soc.*, 2013, **135**, 4412.
12 Y. N. Zhang, J. Hu, M. Law and R. Q. Wu, *Phys. Rev. B: Condens. Matter Mater. Phys.*, 2012, **85**, 085314.

13 N. Berry, M. Cheng, C. L. Perkins, M. Limpinsel, J. C. Hemminger and M. Law, *Adv. Energy Mater.*, 2012, **2**, 1124.
14 H. J. Scheel, *J. Cryst. Growth*, 1974, **24/25**, 669.
15 C. Kloc, G. Willeke and E. Bucher, *J. Cryst. Growth*, 1993, **131**, 448.
16 K. Ellmer and C. Hopfner, *Philos. Mag. A*, 1997, **75**, 1129.
17 J. Luck, A. Hartmann and S. Fiechter, *Fresenius' Z. Anal. Chem.*, 1989, **334**, 441.
18 R. Schieck, A. Hartmann, S. Fiechter, R. Könenkamp and H. Wetzel, *J. Mater. Res.*, 1990, **5**, 1567.
19 G. Willeke, O. Blenk, C. Kloc and E. Bucher, *J. Alloys Compd.*, 1992, **178**, 181.
20 S. W. Lehner, K. S. Savage and J. C. Ayers, *J. Cryst. Growth*, 2006, **286**, 306.
21 S. W. Lehner, N. Newman, M. van Schilfgaarde, S. Bandyopadhyay, K. Savage and P. R. Buseck, *J. Appl. Phys.*, 2012, **111**, 083717.
22 J. Hu, Y. Zhang, M. Law and R. Wu, *Phys. Rev. B: Condens. Matter Mater. Phys.*, 2012, **85**, 085203.
23 H. Fritzsche, *J. Phys. Chem. Solids*, 1958, **6**, 69.
24 B. I. Shklovskii and A. L. Efros, *Electronic Properties of Doped Semiconductors*, Springer, Berlin, 1984.
25 T. Harada, *J. Phys. Soc. Jpn.*, 1998, **67**, 1352.
26 C. H. Ho, Y. S. Huang and K. K. Tiong, *J. Alloys Compd.*, 2006, **422**, 321.
27 C. H. Ho, M. H. Hsieh and Y. S. Huang, *J. Electrochem. Soc.*, 2008, **155**, H254.
28 Y. Tomm, R. Schieck, K. Ellmer and S. Fiechter, *J. Cryst. Growth*, 1995, **146**, 271.
29 M. Cabán-Acevedo, D. Liang, K. S. Chew, J. P. DeGrave, N. S. Kaiser and S. Jin, *ACS Nano*, 2013, **7**, 1731.
30 X. Zhang, M. Manno, A. Baruth, M. Johnson, E. S. Aydil and C. Leighton, *ACS Nano*, 2013, **7**, 2781.
31 S. G. Choi, J. Hu, L. S. Aballah, M. Limpinsel, Y. N. Zhang, S. Zollner, R. Q. Wu and M. Law, *Phys. Rev. B: Condens. Matter Mater. Phys.*, 2012, **86**, 115207.
32 G. Busch and H. Schade, *Lectures on Solid State Physics*, Pergamon, Oxford, 1976.
33 L. Essaleh and J. Galibert, *Phys. Rev. B: Condens. Matter Mater. Phys.*, 1995, **52**, 7798.
34 R. L. Petritz, *Phys. Rev.*, 1958, **110**, 1254.
35 C. L. Perkins, N. Farhi, N. Berry, M. Limpinsel and M. Law, unpublished work.
36 M. Bronold, K. Büker, S. Kubala, C. Pettenkofer and H. Tributsch, *Phys. Status Solidi A*, 1993, **135**, 231.
37 M. Bronold, Y. Tomm and W. Jaegermann, *Surf. Sci.*, 1994, **314**, L931.
38 R. Sun, M. K. Y. Chan and G. Ceder, *Phys. Rev. B: Condens. Matter Mater. Phys.*, 2011, **83**, 235311.
39 H. P. R. Frederikse, W. R. Hosler and D. E. Roberts, *Phys. Rev.*, 1956, **103**, 67.
40 A. Kobayashi, Z. Oda, S. Kawaji, H. Arata and K. Sugiyama, *J. Phys. Chem. Solids*, 1960, **14**, 37.
41 L. F. Lou and W. H. Frye, *J. Appl. Phys.*, 1984, **56**, 2253.
42 T. Thio and J. W. Bennett, *Phys. Rev. B: Condens. Matter Mater. Phys.*, 1994, **50**, 10574.
43 R. E. Jones, K. M. Yu, S. X. Li, W. Walukiewicz, J. W. Ager, E. E. Haller, H. Lu and W. J. Schaff, *Phys. Rev. Lett.*, 2006, **96**, 125505.
44 P. D. C. King, T. D. Veal and C. F. McConville, *J. Phys.: Condens. Matter*, 2009, **21**, 174201.
45 S. M. Sze and K. K. Ng, *Physics of Semiconductor Devices*, Wiley, New York, 3rd edn, 2007.
46 J. R. Ares, A. Pascual, I. J. Ferrer and C. R. Sanchez, *Thin Solid Films*, 2004, **451**, 233.
47 F. W. Herbert, A. Krishnamoorthy, K. J. Van Vliet and B. Yildiz, *Surf. Sci.*, 2013, **618**, 53.
48 W. Folkerts, G. A. Sawatzky, C. Haas, R. A. de Groot and F. U. Hillebrecht, *J. Phys. C: Solid State Phys.*, 1987, **20**, 4135.
49 T. Ollonqvist, R. Perala and J. Vayrynen, *Surf. Sci.*, 1997, **377–379**, 201.
50 L. A. J. Garvie and P. R. Buseck, *Am. Mineral.*, 2004, **89**, 485.
51 I. J. Ferrer, D. M. Nevskaia, C. de las Heras and C. R. Sanchez, *Solid State Commun.*, 1990, **74**, 913.
52 C. de las Heras, I. J. Ferrer and C. Sanchez, *J. Phys.: Condens. Matter*, 1994, **6**, 10177.
53 T. A. Bither, R. J. Bouchard, W. H. Cloud, P. C. Donohue and W. J. Siemons, *Inorg. Chem.*, 1968, **7**, 2208.
54 W. W. Kou and M. S. Seehra, *Phys. Rev. B: Condens. Matter Mater. Phys.*, 1978, **18**, 7062.
55 T.-R. Yang, J.-T. Yu, J.-K. Huang, S.-H. Chen, M.-Y. Tsay and Y.-S. Huang, *J. Appl. Phys.*, 1995, **77**, 1710.
56 A. M. Karguppikar and A. G. Vedeshwar, *Phys. Status Solidi A*, 1988, **109**, 549.
57 *APEX2 Version 2010.9–0*, Bruker AXS, Inc., Madison, WI, 2010.
58 G. M. Sheldrick, *Acta Crystallogr., Sect. A: Found. Crystallogr.*, 2008, **64**, 112.
59 C. L. Perkins and F. S. Hasoon, *J. Vac. Sci. Technol., A*, 2006, **24**, 497.

 